ADVANCED FUNCTIONAL MATERIALS
www.afm-journal.de

Atomic Modulation and Structure Design of Fe–N_4 Modified Hollow Carbon Fibers with Encapsulated Ni Nanoparticles for Rechargeable Zn–Air Batteries

Yuhui Tian, Zhenzhen Wu, Meng Li, Qiang Sun, Hao Chen, Ding Yuan, Daijie Deng, Bernt Johannessen, Yun Wang, Yulin Zhong, Li Xu, Jun Lu, and Shanqing Zhang**

Excellent bifunctional oxygen reduction reaction (ORR)/oxygen evolution reaction (OER) activity and rapid mass transport capability are two important parameters of electrocatalysts for high-performance rechargeable Zn–air batteries (ZABs). Herein, an efficient atomic modulation and structure design to promote bifunctional activity and mass transport kinetics of an ORR/OER electrocatalyst are reported. Specifically, atomic Fe–N_4 moieties are immobilized on premade hollow carbon fibers with encapsulated Ni nanoparticles (Fe-N@Ni-HCFs). Synchrotron X-ray absorption spectroscopy and spherical aberration-corrected electron microscope analyses confirm the atomic distribution of the active sites and unique lung bubble-like hollow architecture of the catalyst, while theoretical investigations reveal that the encapsulated Ni nanoparticles can induce electron distribution of the atomic Fe–N_4 moieties to reduce reaction energy barriers. As a result, the prepared catalyst possesses enhanced bifunctional ORR/OER activity and well-constructed gas–solid–liquid interfaces for improved mass transfer. These synergetic advantages endow the binder-free Fe-N@Ni-HCFs electrode with the remarkable power density and cycling stability for ZABs, outperforming the commercial Pt/C+Ir/C benchmark. This exceptional performance suggests that the proposed strategy can be extended to the design and fabrication of electrocatalysts for energy conversion and storage.

1. Introduction

Electrochemical energy conversion and storage technologies constitute key components for the next-generation energy structure that integrates renewable sources for a reliable and flexible power supply with a low carbon footprint.[1] Zn–air batteries (ZABs), one of the most promising technologies, can generate electricity via the redox reaction between oxygen (O_2) from ambient air and a Zn anode with zero carbon emission, thus meeting the requirements of a low-carbon economy.[2] The performance of ZABs is strongly dependent on the electrochemical oxygen reduction reaction (ORR) and oxygen evolution reaction (OER) occurring at the air electrode.[3] However, the sluggish kinetics of both ORR and OER result in large charge–discharge polarization, low energy efficiency, and early cell death.[4] Thus, efficient electrocatalysts are required to accelerate redox kinetics at the cathode, reduce the reaction energy barrier, and prolong the cycling lifespan.

Y. Tian, Z. Wu, M. Li, H. Chen, D. Yuan, Y. Wang, L. Xu, S. Zhang
Centre for Catalysis and Clean Energy
School of Environment and Science
Gold Coast Campus
Griffith University
Queensland 4222, Australia
E-mail: s.zhang@griffith.edu.au

Z. Wu
Key Laboratory of Advanced Material Processing & Mold
Ministry of Education
Zhengzhou University
Zhengzhou 450002, P. R. China

The ORCID identification number(s) for the author(s) of this article can be found under https://doi.org/10.1002/adfm.202209273.

DOI: 10.1002/adfm.202209273

M. Li, Y. Zhong
Queensland Micro- and Nanotechnology Centre
Nathan Campus
Griffith University
Brisbane, Queensland 4111, Australia

Q. Sun
Centre for Microscopy and Microanalysis
University of Queensland
Brisbane, Queensland 4072, Australia

D. Deng, L. Xu
Institute for Energy Research
School of Chemistry and Chemical Engineering
Key Laboratory of Zhenjiang
Jiangsu University
Zhenjiang 212013, P. R. China

B. Johannessen
Australia Synchrotron
Australia's Nuclear Science and Technology Organization
Victoria 3168, Australia

J. Lu
College of Chemical and Biological Engineering
Zhejiang University
Hangzhou, Zhejiang Province 310027, P. R. China
E-mail: junzoelu@zju.edu.cn

Ideally, the most desirable electrocatalysts for rechargeable ZABs should be highly active and robust in catalyzing both ORR and OER at low overpotentials with long-term durability.[5] However, the ORR and OER comprise distinct elementary reactions, have different rate-determining steps, and thus require different electrocatalysts to accelerate the reaction process.[6] Electrocatalysts composed of a single type of active moiety typically fail to meet ORR/OER bifunctionality requirements.[6] Using composite electrodes integrated with ORR and OER active sites can help overcome this challenge.[7] However, the integrated ORR and OER active sites compete to occupy the most efficient positions on the catalytic surface for their respective pathways.[8] Consequently, the number of ORR and OER active sites is restricted, resulting in insufficient utilization of the active surface for each reaction. Moreover, adverse interferences may be induced by integrated multicomponent active species, thereby decreasing the catalytic efficiency.[8] Therefore, rationally regulating the arrangement of active species and enhancing the utilization efficiency of the active region should be strictly considered for constructing advanced composite electrocatalysts.

Active sites can be effectively regulated by manipulating the atomic composition and engineering the electronic structure to promote intrinsic bifunctional ORR/OER activity.[9] However, optimizing only the active species of electrocatalysts is not sufficient. Electrocatalytic processes in rechargeable ZABs involve electron transfer, O_2 gas diffusion, and ion transport at the O_2 (gas)–electrolyte (liquid)–catalyst (solid) interface. An unstable triple-phase environment on the air electrode causes unfavorable mass transport, increased ohmic resistance, and loss of the effective reaction zone during long-term operation.[10] Together, these factors significantly limit the practical performance of ZABs. In this regard, endowing the electrode nanoarchitecture and interfacial structure with high porosity and appropriate hydrophilicity to form a desirable triple-phase interface should be considered to enhance the overall performance of ZABs.[2]

The pilot fabrication of air electrodes for ZABs is mainly based on the conventional slurry coating method. In this method, the electrocatalyst and binder additives are mixed to form a slurry and subsequently loaded onto conductive substrates via drop casting. The inner resistance inevitably increases owing to the nonconductive nature of the binder additives.[11] Some active sites in the micropores might be blocked and inaccessible to the electrolyte, thus deteriorating the catalytic efficiency.[12] Mass transport will also be suppressed owing to the decreased number of transport microchannels, which, in turn, will inhibit the diffusion of O_2 and ions. Moreover, electrocatalyst stripping due to binder deactivation during operation will result in attenuated performance and reduced lifespan of ZABs.[13] Therefore, it is of great significance to design and fabricate binder-free air cathodes integrated with highly active species to reduce the discharge-charge overpotential and realize a well-optimized open-pore structure to promote mass transport, thus overcoming the challenges in further development of ZABs.

Herein, we demonstrate a proof-of-concept for optimizing the electrocatalytic activity and promoting the mass transport of the electrocatalyst via rational atomic modulation and structure design. A fibrous carbon composite fabricated by electrospinning exhibited a unique hierarchical lung bubble-like hollow architecture. Synchrotron X-ray absorption spectroscopy (XAS) and spherical aberration-corrected electron microscopy analyses suggested that atomic Fe–N_4 moieties were immobilized onto hollow carbon fibers with encapsulated Ni nanoparticles (Fe-N@Ni-HCFs). Theoretical and electrochemical investigations revealed that the Fe–N_4/Ni composite sites with altered electronic configurations contributed to the enhanced ORR and OER activities. Importantly, the lung-bubble-like hollow architecture facilitated the formation of ample gas–solid–liquid interfaces and promoted mass transfer. Owning to the enhanced bifunctional activity and mass transfer, the binder-free Fe-N@Ni-HCFs electrode endowed the assembled liquid-state and quasi-solid-state (QSS) ZABs with excellent rechargeability, high peak power density, and satisfactory cycling stability.

2. Results and Discussion

2.1. Theoretical Calculations

Previous theoretical and experimental investigations have suggested that well-defined Fe–N_4 moieties in Fe–N–C single-atom catalysts (SACs) are thermodynamically stable and can serve as active sites to deliver exceptional ORR activity that is comparable to the noble metal Pt/C catalyst.[14] Nonetheless, it has been proposed that the best ORR catalyst does not usually offer the optimum OER activity.[6] Thus, the OER activity of Fe–N–C SACs should be further optimized while maintaining a high ORR activity.

In addition to the surrounding heteroatoms, organic ligands, and anionic guest groups (e.g., Cl^-, SCN^-, or CN^-), inorganic metal nanoparticles or clusters can interact with the central metal atom in M—N—C (M = metal atom) SACs.[15] Electron-rich metallic species can be more effective for tuning the electronic structure of atomic moieties and improving the intrinsic electrocatalytic activity through electronic coupling.[16] To this end, we have proposed to promote the ORR/OER catalytic activity of the Fe–N–C catalyst by introducing the metallic Ni nanoparticles.

Density functional theory (DFT) calculations were performed to evaluate the possibility and clarify the specific role of metallic Ni in influencing the catalytic properties. The theoretical model (**Figure 1**a) consisted of an atomic Fe–N_4 site-embedded graphene monolayer on the Ni(111) surface (denoted as Fe–N_4–C||Ni). The Ni(111) plane was adopted due to its good compatibility and minor lattice mismatch with respect to graphene.[17] Compared with bare Fe–N_4–C, the Fe center's partial density of states (PDOS) in Fe–N_4–C||Ni showed a negative shift (Figure 1b). Higher electronic states neighboring the Fermi level were achieved on Fe–N_4–C||Ni, suggesting higher reactivity and electron mobility.[18] Moreover, the corresponding *d*-band center of Fe in Fe–N_4–C||Ni (–1.19 eV) exhibited a downshift compared to bare Fe–N_4–C (–1.00 eV), implying a weakened affinity toward oxygen-containing intermediates.[19] The charge density difference (Figure 1c) revealed significant charge redistribution on the Ni(111) surface and graphene wall. The transferred charge was

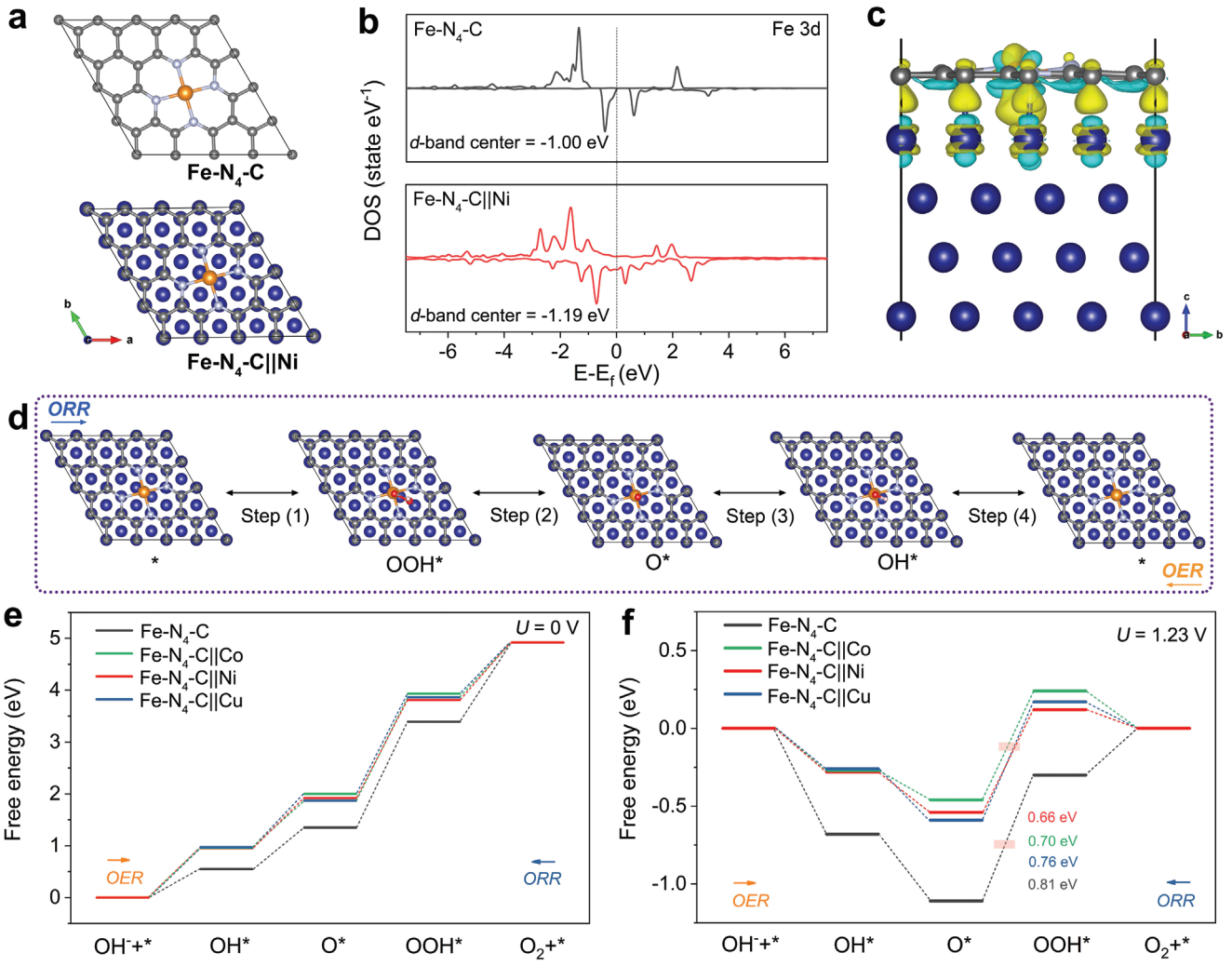

Figure 1. a) The optimized structure models of Fe–N_4–C (top) and Fe–N_4–C||Ni (below). b) PDOS of Fe atom in Fe–N_4–C and Fe–N_4–C||Ni. c) The differential charge density of Fe–N_4–C||Ni (the isosurface value is set to be 0.005 eÅ^{-1}, and the charge accumulation and depletion areas are shown in yellow and cyan, respectively). d) The optimized geometrical structures of OOH*, O*, and OH* on Fe–N_4–C||Ni. Color code: H, C, N, O, Ni, and Fe atoms are represented in pink, grey, silver, red, blue, and orange, respectively. Free energy diagrams of different intermediates on Fe–N_4–C, Fe–N_4–C||Co, Fe–N_4–C||Ni and Fe–N_4–C||Cu models at e) $U = 0$ V and f) $U = 1.23$ V.

delocalized on the interface. Bader charge analysis showed that the Fe atom in Fe–N_4–C lost 1.09|e| to the surrounding N–C. In contrast, the Fe in Fe–N_4–C||Ni lost only 0.93|e|, suggesting that electrons were transferred from Ni to Fe via interfacial interactions or through the graphene layer. Changes in the electronic structure indicated the altered intrinsic activity toward the ORR and OER.[17]

Gibbs free energies (ΔG) were calculated based on the typical four-electron transfer pathway for the ORR/OER, involving OH*, O*, and OOH* intermediates. For comparison, Fe–N_4–C||Co and Fe–N_4–C||Cu models were also constructed by replacing Ni(111) with Co(111) and Cu(111) planes owning to their similar lattice parameters.[20] The optimized atomic structures with oxygenated intermediates are illustrated in Figure 1d and Figure S1 (Supporting Information). The limiting reaction barriers were compared to evaluate their catalytic activity. At an electrode potential (U) of 0 V (Figure 1e), the smallest downhill in the last elementary step of the ORR indicates that the rate-determining step (RDS) was the final removal of OH* for Fe–N_4–C.[19,21] With the metal substrates, the ΔG_{OH*} was more significant than that of the bare Fe–N_4–C (Table S1, Supporting Information), suggesting easier desorption of OH*. The accelerated desorption step of intermediates was beneficial for regenerating the active sites, thus achieving a higher reaction efficiency.[22] At $U = 1.23$ V (Figure 1f), the more negative free energy on bare Fe–N_4–C indicated more robust interactions between active sites and intermediates. When transition metals were introduced, the binding strength decreased for all the intermediates. The energy barrier involved in the formation of OOH* for OER was lower with Fe–N_4–C||Ni (0.66 eV) than with Fe–N_4–C (0.81 eV). Although a similar enhancement effect was observed on Fe–N_4–C||Co and Fe–N_4–C||Cu for ORR, considerable energy barriers of 0.70 and 0.76 eV were required, respectively, for forming OOH* during OER. These results revealed that incorporating metallic Ni could significantly influence the ORR and OER energetics of the Fe–N_4 site by modulating

the electronic structure, resulting in more favorable reaction kinetics for oxygen electrocatalysis.

2.2. Catalyst Synthesis and Characterizations

Based on the theoretical investigations, atomic Fe–N_4-modified hollow carbon fibers with encapsulated Ni nanoparticles were fabricated experimentally. The multistep fabrication process is illustrated in **Figure 2**a. Pre-synthesized nano-cuboid Ni precursors with a size of ≈400 nm (Figure S2, Supporting Information) were dispersed into the dimethylformamide (DMF) solution containing polyacrylonitrile (PAN) to obtain the hybrid precursor solution. Ni-containing PAN fibers (Ni@PFs), in which Ni precursors were uniformly confined within the PAN fibers, were then fabricated by electrospinning (Figure S3, Supporting Information). High-temperature carbonization converted PAN into graphitic carbon. Meanwhile, the Ni precursors were reduced in situ to form metallic Ni nanoparticles (Figure S4, Supporting Information). The resultant sample (Ni_{NP}@Ni-HCFs) maintained a fibrous structure with irregular protuberances (Figure S5a, Supporting Information). Lotus root-like channels were observed at the cross-section, indicating the formation of inner hollow voids (Figure S5b, Supporting Information). Subsequently, the Fe–N_4 moieties were modified through wet impregnation using Fe^{2+} ions and 1,10-phenanthroline (Phen), which formed Fe-Phen complexes that were adsorbed on the premade carbon fibers. The Fe-N@Ni-HCFs catalyst with good

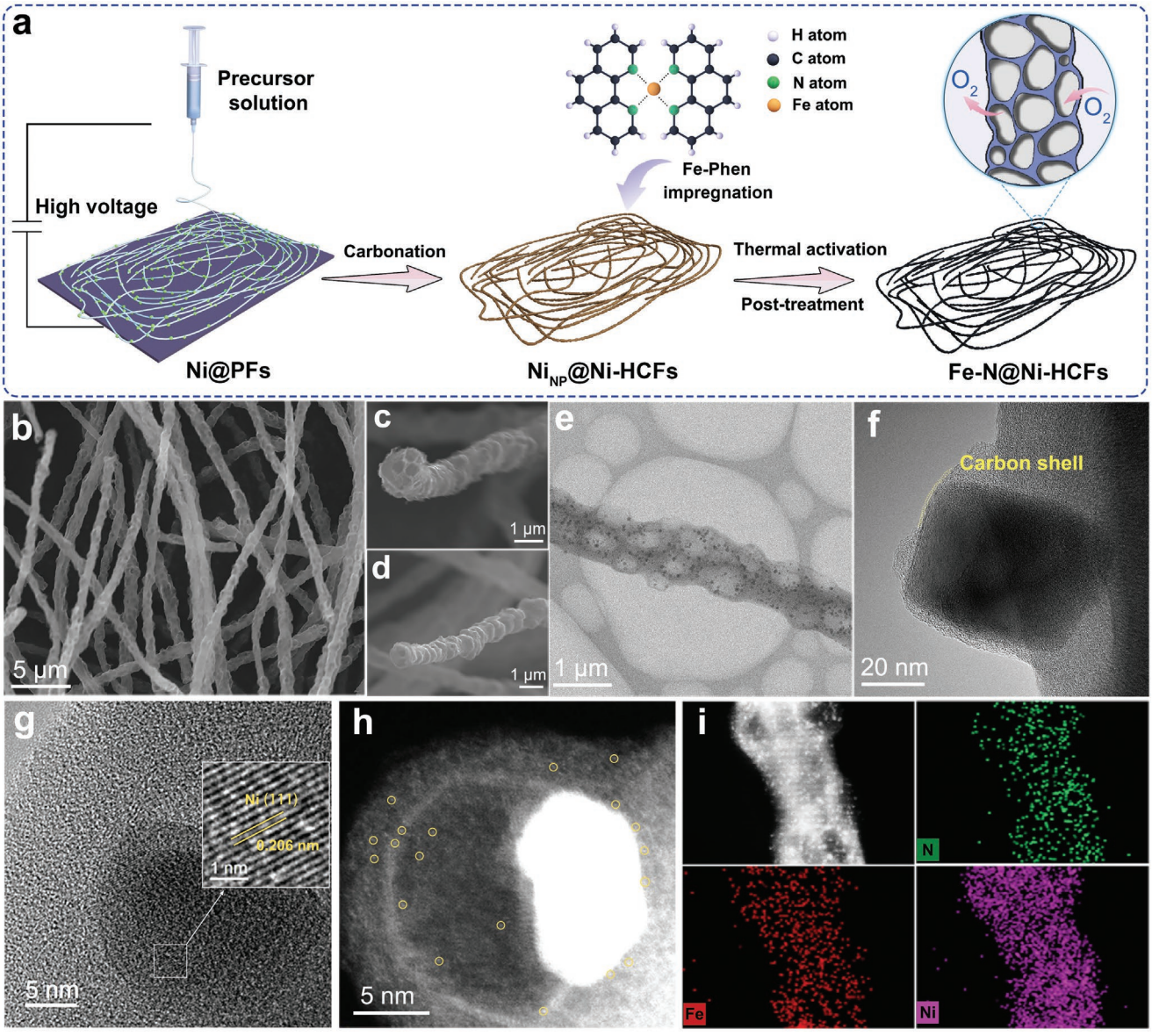

Figure 2. a) Schematic illustration for the fabrication procedure of Fe-N@Ni-HCFs. b–d) SEM images, e,f) TEM images, g) HRTEM image (inset: enlarged image of the selected region), and h) aberration-corrected HAADF-STEM image of Fe-N@Ni-HCFs. i) HAADF-STEM image and corresponding elemental mapping of Fe-N@Ni-HCFs.

flexibility and the robust mechanical property was obtained after further thermal activation and post-treatment (Figure S6, Supporting Information). Control samples (i.e., Ni-HCFs and Fe-N@CFs) were also fabricated for comparison (see Experimental Section in the Supporting Information).

The existence of metallic Ni within the carbon framework was confirmed by the X-ray diffraction (XRD) patterns of Ni-HCFs and Fe-N@Ni-HCFs (Figure S7, Supporting Information). Three sharp diffraction peaks at ≈44.5°, 51.8°, and 76.4° were identified, corresponding to the (111), (200), and (220) planes of Ni^0 (JCPDS No. 04–0850), respectively.[23] The broad peak at 25.8° originated from the (002) plane of graphitic carbon. No diffraction peaks of crystalline Fe species were observed for Fe-N@Ni-HCFs and Fe-N@CFs. Inductively coupled plasma-mass spectrometry revealed that the Fe and Ni contents in Fe-N@Ni-HCFs were 1.11 wt.% and 25.27 wt.%, respectively. The much lower Fe content suggests the atomic dispersion of Fe species within the catalyst. Raman spectra (Figure S8, Supporting Information) showed broad D and G vibrational bands with similar intensity ratios (I_D/I_G) for all the synthesized samples, indicating the similarity of their defective and graphitic carbon structures. The porosity of Fe-N@Ni-HCFs was investigated by the N_2 adsorption-desorption isotherm. The Brunauer-Emmett-Teller surface area was determined to be 283.6 $m^2\ g^{-1}$. The type-IV isotherm and different mesopore distribution (Figure S9, Supporting Information) confirmed the mesoporous structure of the Fe-N@Ni-HCFs catalyst.

The morphologies of Ni-HCFs, Fe-N@CFs, and Fe-N@Ni-HCFs were compared based on field-emission scanning electron microscopy (FE-SEM) images. The fibrous architecture was well maintained for Fe-N@Ni-HCFs (Figure 2b) and Ni-HCFs (Figure S10, Supporting Information). Moreover, the lotus root-like channels at the cross-section were well preserved (Figure 2c,d). A porous structure with a hollow interior is expected to expose more active sites and simultaneously provide ample channels for efficient O_2 diffusion and rapid ion transport during oxygen electrocatalysis.[13] In contrast, the fibrous Fe-N@CFs catalyst exhibited a smooth surface and a solid core at the cross-section (Figure S11, Supporting Information). The formation of inner space led to a larger fiber diameter of Fe-N@Ni-HCFs and Ni-HCFs than that of Fe-N@CFs.

The transmission electron microscopy (TEM) image of Fe-N@Ni-HCFs (Figure 2e) showed the lung bubble-like cavities inside the carbon fibers. In addition, Ni nanoparticles were homogeneously dispersed within the porous carbon framework. The size distribution (Figure S12, Supporting Information) showed that most Ni particles ranged from 20 to 60 nm. The broad particle size distribution could be caused by the particle coalescence and/or Ostwald processes during the thermal treatment.[24] As seen in Figure 2f, the nanoparticle was fully encapsulated by graphitic carbon, inducing bulges on the carbon fiber surface. A single-layer graphitic carbon shell was presented, wherein incorporated atomic Fe–N_x sites could interact with encapsulated Ni via electronic coupling. The high-resolution TEM (HRTEM) image in Figure 2g showed a well-resolved lattice fringe of 0.206 nm in the encapsulated nanoparticle, in good agreement with the Ni(111) facet spacing.[23] The spherical aberration-corrected high-angle annular dark-field scanning transmission electron microscopy (HAADF-STEM) image in Figure 2h showed the atomically isolated bright spots (highlighted with yellow circles) in the hollow carbonaceous framework. The electron energy loss spectrum (EELS) collected in the nanoparticle region showed a pair of peaks corresponding to the Ni L_2 and L_3 edges (Figure S13, Supporting Information). The bright dots were identified as Fe co-existing with N at the atomic level, verifying the formation of atomic Fe–N_x species in the carbon matrix.[25] Ni signal was not observed in the selected region, excluding the possible existence of atomic Ni. The densely dispersed Fe–N_x moieties throughout the carbon matrix could contribute to a good ORR activity of the catalyst. Moreover, atomic Fe sites were also observed near the Ni nanoparticles, indicating the presence of Fe–N_x/Ni composite sites, which could deliver enhanced OER activity compared to bare Fe–N_x sites. The energy-dispersive spectroscopy (EDS) mapping of the Fe-N@Ni-HCFs catalyst demonstrated a uniform distribution of C, N, Fe, and Ni within the carbon fibers (Figure 2i). The elemental distribution of Ni-HCFs and Fe-N@CFs obtained by SEM elemental mappings are shown in Figures S14 and S15 (Supporting Information), respectively.

The chemical compositions and surface chemical states of prepared samples were investigated by X-ray photoelectron spectroscopy (XPS). The high-resolution C 1s spectra (Figure S16, Supporting Information) of all three samples showed C−C/C=C, C−N, C−O/C=O, and O−C=O subpeaks, which commonly exist in N-doped carbon materials.[26] The N 1s spectra (Figure S17, Supporting Information) could be deconvoluted into three peaks: pyridinic N (398.5 eV), pyrrolic N (399.7 eV), and graphitic N (401.0 eV).[27] Pyridinic N has been widely reported to participate in the formation of Fe–N_x species and optimize the local electronic structure to enhance electrocatalytic activity.[27,28] It is evident that a higher percentage of pyridinic N is present in Fe-N@CFs (42.0%) and Fe-N@Ni-HCFs (46.7%) compared to Ni-HCFs (31.8%), suggesting the incorporation of Fe–N_x moieties.[27] The Fe 2p XPS spectrum (Figure S18, Supporting Information) of Fe-N@Ni-HCFs exhibited two subpeaks at ≈711.2 and ≈724.4 eV, which can be indexed to the Fe 2p3/2 and Fe 2p1/2 orbitals, respectively.[29] The binding energy of Fe-N@Ni-HCFs in the Fe 2p spectrum was slightly negatively shifted relative to that of Fe-N@CFs, indicating an increased charge density of Fe in Fe-N@Ni-HCFs.[30] The high-resolution Ni 2p spectra of Ni-HCFs and Fe-N@Ni-HCFs (Figure S19, Supporting Information) showed typical peaks of metallic Ni, with the Ni $2p_{3/2}$ peak at ≈854.9 eV and Ni $2p_{1/2}$ peak at ≈872.3 eV, in addition to their satellite peaks.[31] The Ni 2p spectrum of Fe-N@Ni-HCFs shifted slightly to higher binding energy relative to that of Ni-HCFs. Echoing the negative shift of the Fe 2p spectrum, it indicated the existence of electronic interactions between metallic Ni and atomic Fe in the Fe-N@Ni-HCFs. The electron transfer from Ni to adjacent Fe–N_x sites led to an increased electron density in the Fe atoms, consistent with DFT calculations.[16a]

To obtain more accurate electronic states and local coordination environments of Fe and Ni in Fe-N@Ni-HCFs, synchrotron-based X-ray absorption spectroscopy (XAS) was performed. The Fe K-edge X-ray absorption near-edge structure (XANES) spectra of Fe-N@Ni-HCFs and the reference samples (**Figure 3**a) showed that the Fe pre-edge position of Fe-N@Ni-HCFs lay between that of FeO and Fe_2O_3, although relative closer to

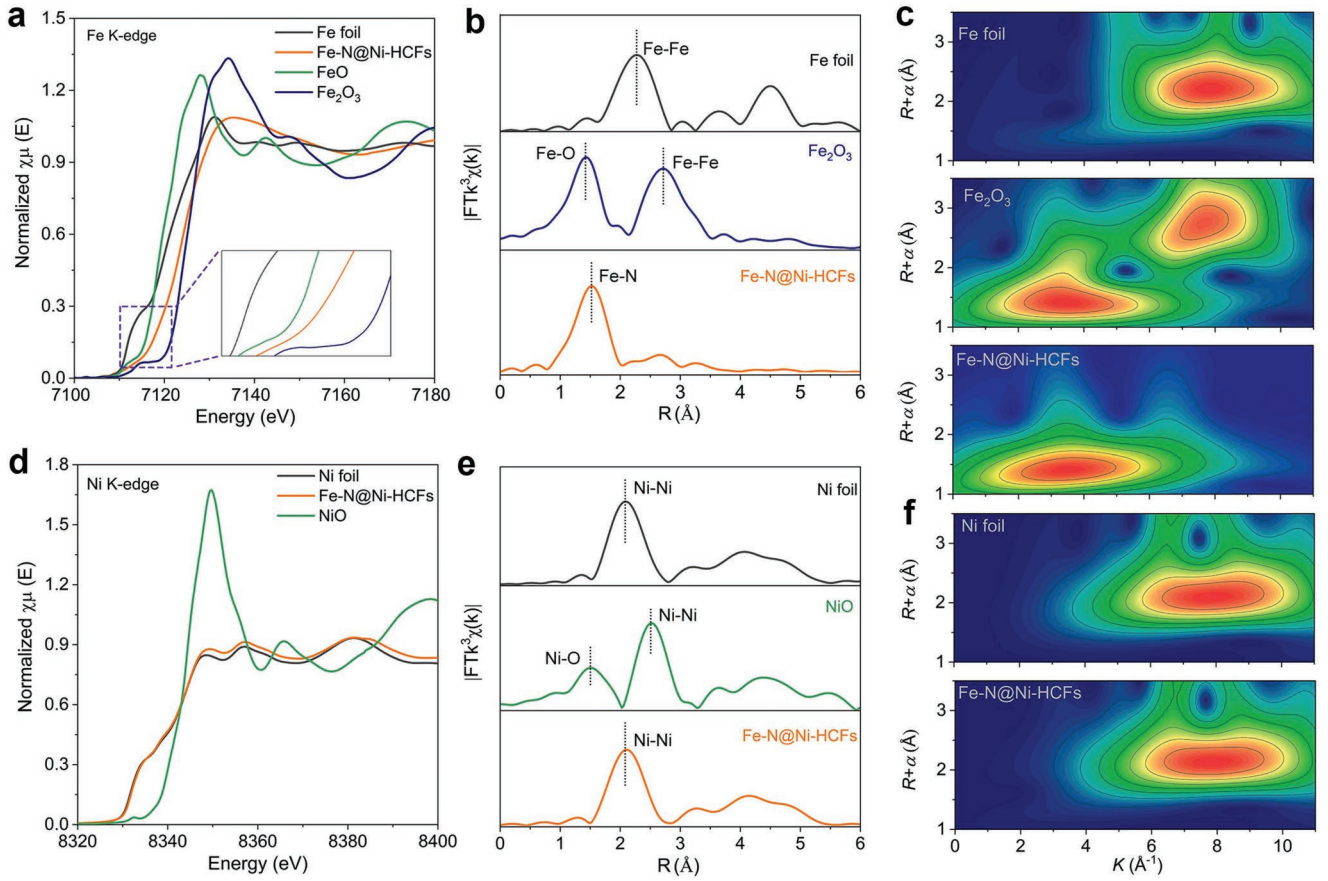

Figure 3. a) Fe K-edge XANES spectra of Fe-N@Ni-HCFs and reference samples (Fe foil, FeO, and Fe_2O_3). b) Fe K-edge FT-EXAFS curves of Fe foil, Fe_2O_3, and Fe-N@Ni-HCFs. c) Wavelet transform of EXAFS (WT-EXAFS) contour plots of Fe foil, Fe_2O_3, and Fe-N@Ni-HCFs. d) Ni K-edge XANES spectra of Fe-N@Ni-HCFs and reference samples (Ni foil and NiO). e) Ni K-edge FT-EXAFS curves of Ni foil, NiO, and Fe-N@Ni-HCFs. f) WT-EXAFS contour plots of Ni foil and Fe-N@Ni-HCFs.

FeO. This indicates the existence of positively charged Fe atoms ($2 < \delta < 3$). Fourier transformed extended X-ray absorption fine structure (FT-EXAFS) spectrum of Fe-N@Ni-HCFs showed a prominent peak at 1.5 Å, which is typical of Fe–N scattering (Figure 3b).[32] Wavelet transform (WT) was used to analyze the variation in the local bonding environment of Fe in Fe-N@Ni-HCFs and the reference samples. The WT-EXAFS contour plot of Fe-N@Ni-HCFs was distinct from those of the bulk crystalline Fe foil and Fe_2O_3 (Figure 3c). The single WT intensity maximum at ≈4.0 $Å^{-1}$ for Fe-N/HCFs was assigned to the contribution of Fe–N, further reflecting the isolated distribution of Fe atoms within the carbon fibers.[33] The Ni K-edge XANES spectrum of Fe-N@Ni-HCFs was similar to that of bulk Ni foil (Figure 3d). The FT-EXAFS spectrum confirmed the presence of Ni–Ni bonds (Figure 3e). This was also supported by the WT-EXAFS contour plots (Figure 3f), wherein the intensity maxima of Fe-N@Ni-HCFs and Ni foil at ≈7.9 $Å^{-1}$ represented the Ni–Ni scattering path.[34] No signals corresponding to other Ni moieties (e.g., Ni–N/O) were detected, indicating the metallic state of Ni in Fe-N@Ni-HCFs rather than single-atomic Ni sites, in agreement with the XRD and EELS analyses. The FT-EXAFS curve of Fe-N@Ni-HCFs was fitted to quantitatively determine the coordination configuration of Fe in Fe-N@Ni-HCFs. The fitting curves in *R* space and *k* space are presented in Figures S20 and S21 (Supporting Information), respectively, and the fitting parameters are listed in Table S2 (Supporting Information). Fitting analyses suggested that the Fe atom was surrounded by four N atoms in the first shell. Hence, the above comprehensive characterizations unambiguously demonstrate the hollow fiber structure of Fe-N@Ni-HCFs containing encapsulated Ni nanoparticles and atomically dispersed $Fe–N_4$ sites.

2.3. Electrochemical Performances

The bifunctional ORR and OER performances of Fe-N@Ni-HCFs and the reference samples, including commercial Pt/C (20 wt.%) and Ir/C (20 wt.%) catalysts, were evaluated in 0.1 M KOH using the three-electrode system. All the potentials were calibrated to the reversible hydrogen electrode (RHE). The cyclic voltammetry (CV) curves for all samples show visible cathodic peaks in the potential range of 0.7–1.0 V (vs RHE) in an O_2-saturated electrolyte, whereas no redox peaks were observed in the electrolyte saturated with N_2, verifying the ORR catalytic capability of the catalysts (Figure S22, Supporting Information). The more positive cathodic peak of Fe-N@Ni-HCFs compared

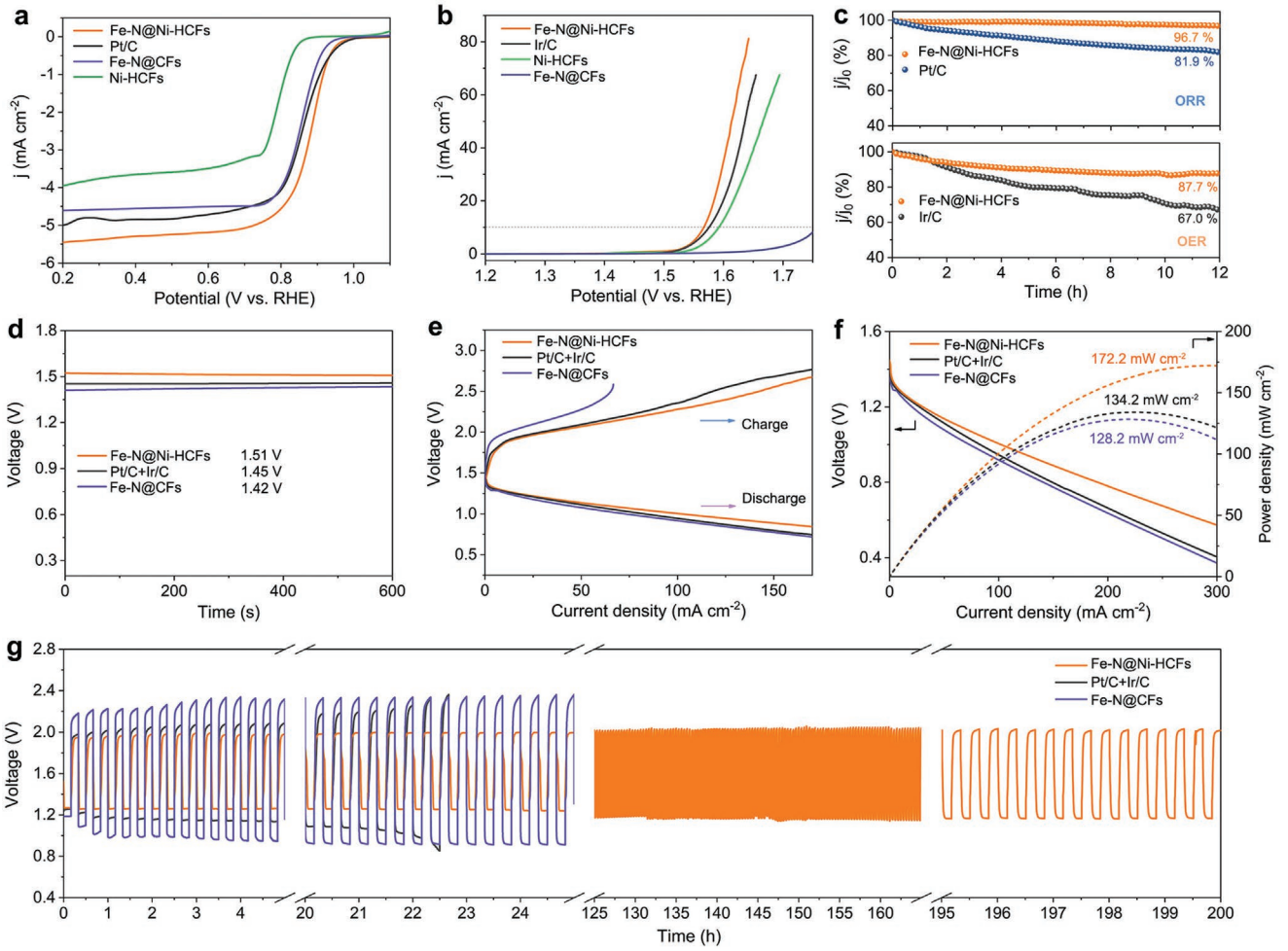

Figure 4. a) ORR LSV curves of Ni-HCFs, Fe-N@CFs, Fe-N@Ni-HCFs, and Pt/C in O_2-saturated 0.1 M KOH under a rotation rate of 1600 rpm. b) OER LSV curves of Ni-HCFs, Fe-N@CFs, Fe-N@Ni-HCFs, and Ir/C in 0.1 M KOH under a rotation rate of 1600 rpm. c) Chronoamperometric curves of Fe-N@Ni-HCFs for ORR and OER. d) OCV plots of the assembled liquid ZABs. e) Discharge and charge polarization curves of the liquid ZABs, and f) the corresponding power density plots. g) Galvanostatic discharge–charge curves at 10 mA cm^{-2}.

to those of the control samples indicated the better ORR activity of the former.[27] The ORR linear sweep voltammetry (LSV) curve of Fe-N@Ni-HCFs (**Figure 4**a) showed a half-wave potential ($E_{1/2}$) of 0.88 V, which was superior to those of Ni-HCFs (0.79 V), Fe-N@CFs (0.85 V), and Pt/C (0.86 V). Meanwhile, the higher limiting current density (j_L) of Fe-N@Ni-HCFs compared to those of Fe-N@CFs and Pt/C indicated excellent mass transfer performance. The Tafel slope of Fe-N@Ni-HCFs (53.1 mV dec^{-1}) was smaller than those of the control samples (56.2 mV dec^{-1} for Ni-HCFs, 61.6 mV dec^{-1} for Fe-N@CFs, and 78.2 mV dec^{-1} for Pt/C), reflecting its superior ORR reaction kinetics (Figure S23, Supporting Information). The electron transfer number (n) for the ORR was calculated according to the Koutecky–Levich (K–L) equations using LSV curves at different rotation speeds (Figure S24, Supporting Information). The excellent linearity and parallelism of the K–L plots in the potential range of 0.2–0.6 V suggested the first-order reaction kinetics of Fe-N@Ni-HCFs with respect to the concentration of dissolved O_2 in the electrolyte.[35] The n value was calculated to be 3.93 for Fe-N@Ni-HCFs. The rotating ring disk electrode (RRDE) was further employed to quantitatively investigate the n and HO_2^- yields. In the potential range of 0.2–0.8 V (vs RHE), the HO_2^- yield of Fe-N@Ni-HCFs was below 8% (Figure S25, Supporting Information). The corresponding electron transfer number was 3.85–3.98, which was comparable to that of the Pt/C benchmark (3.87–3.96). Combining the analyses using the K–L equations and the results of the RRDE tests, a four-electron ORR pathway was demonstrated for Fe-N@Ni-HCFs.

The OER catalytic activity is presented in Figure 4b. The Fe-N@Ni-HCFs catalyst required a small overpotential of 337 mV to reach a current density of 10 mA cm^{-2}, which was 9 and 25 mV lower than those required by Ir/C and Ni-HCFs, respectively. The OER activity of Fe-N@CFs was much inferior due to the lack of efficient active sites. The Tafel plots (Figure S26, Supporting Information) extracted from the LSV curves had a smaller slope for Fe-N@Ni-HCFs (54.7 mV dec^{-1}) than for Ir/C (73.3 mV dec^{-1}) and Ni-HCFs (69.9 mV dec^{-1}), reflecting the excellent reaction kinetics of Fe-N@Ni-HCFs for the OER. Electrochemical impedance spectroscopy (EIS) was performed to investigate the charge-transfer resistance during

the OER. In the EIS Nyquist plots (Figure S27, Supporting Information), the smallest semicircle for Fe-N@Ni-HCFs suggested a lower charge transfer resistance and more efficient charge transport than those of the control samples.[35]

The bifunctional activity can be quantified from the potential difference (ΔE) between $E_{1/2}$ for the ORR and the potential required to generate the current density of 10 mA cm^{-2} for the OER ($E_{j\,=\,10}$). A smaller value of ΔE indicates superior reversibility. The ΔE value of Fe-N@Ni-HCFs (0.687 V) was lower than that of the Pt/C+Ir/C couple (0.722 V). Moreover, the bifunctional ORR/OER activity of Fe-N@Ni-HCFs surpassed that of many of the recently reported state-of-the-art bifunctional electrocatalysts (Table S3, Supporting Information). The electrochemical stability of Fe-N@Ni-HCFs was examined through the continuous operation of the ORR and OER at the applied potentials of 0.4 and 1.60 V (vs RHE), respectively. Pt/C and Ir/C catalysts were tested under identical conditions for comparison. Fe-N@Ni-HCFs catalyst exhibited good ORR and OER durability, with minor current degradation (Figure 4c). In contrast, commercial Pt/C and Ir/C catalysts showed severe degradation of current density. This clearly demonstrated the superior electrochemical stability of Fe-N@Ni-HCFs.

To identify the active sites in the Fe-N@Ni-HCFs composite, the ORR and OER performances were further evaluated in 0.1 M KOH containing KSCN. SCN^- ions tend to bind to the M–N_x sites, thereby degrading the catalytic performance of M—N—C SACs.[36] Figure S28 in the Supporting Information shows the LSV curves obtained for Ni-HCFs and Fe-N@Ni-HCFs in the presence and absence of SCN^-. The Fe-N@Ni-HCFs catalyst showed considerable performance decay in the SCN^--containing electrolyte, indicating that exposed atomic Fe–N_4 sites were the main active species in both ORR and OER. In contrast, negligible change in the ORR/OER activity was observed for Ni-HCFs after adding SCN^-. This suggested that the Ni nanoparticles in Fe-N@Ni-HCFs did not participate directly in electrocatalytic reactions because of the carbon layer coating; they could, however, optimize the electrocatalytic activity of the Fe–N_4 sites.

Double-layer capacitances (C_{dl}) were analyzed as the descriptor to evaluate the electrochemically active surface areas (Figure S29, Supporting Information). Fe-N@Ni-HCFs catalyst exhibited a higher C_{dl} value (24.4 mF cm^{-2}) than the control samples (17.7 mF cm^{-2} for Ni-HCFs and 5.4 mF cm^{-2} for Fe-N@CFs), indicating that more electroactive surfaces were exposed in Fe-N@Ni-HCFs. In contrast to Fe-N@CFs, the active region in Fe-N@Ni-HCFs was not constrained by the surface of the outer layer. The porous hollow structure with lotus root-like channels at the cross-section and lung bubble-like cavities in the interior provided a greater number of accessible active sites, significantly increasing the area of the active region.

In rechargeable ZABs, the mass transfer occurs mainly via O_2 diffusion and the transport of ions at the triple-phase interface. The excellent mass transport capability of the air electrode can reduce the mass transfer-related concentration polarization in rechargeable ZABs.[37] The underwater wettability of the catalyst layer is closely related to the nature of gas–liquid–solid interfaces, which significantly affects the overall mass transfer performance.[38] Since water molecules and hydroxide ions in the aqueous electrolyte also participate in the electrocatalytic ORR/OER, a hydrated environment around the active sites is essential. However, complete wetting of the catalyst layer would cause water flooding of the active sites, with negligible air cushion between the electrolyte and electrode.[10] In contrast, a highly hydrophobic nature would reduce the electrolyte–catalyst contact, limiting the accessibility of the active sites to the electrolytes. Both cases restrain the electrocatalytic performance. Therefore, appropriate hydrophilicity of the catalyst layer is important for optimizing the overall ZAB performance. The surface wetting state of Fe-N@Ni-HCFs was assessed by the contact angle (CA) test. For comparison, a hydrophobic carbon cloth was modified with Pt/C+Ir/C catalysts using Nafion as the binder to fabricate the Pt/C+Ir/C electrode. The Fe-N@CFs electrode was hydrophobic in nature, with a water contact angle of 145° (Figure S30). This, perhaps, resulted in poor electrolyte–catalyst contact. The Pt/C+Ir/C electrode exhibited a contact angle of ≈95°, suggesting enhanced surface wetting. However, this also increased the possibility of water flooding. The Fe-N@Ni-HCFs electrode presented a moderate surface wetting state with a contact angle of ≈ 119°. Thus, the electrolyte can partly wet the catalyst layer and prevent the complete soaking, thereby shortening the gas transport path and maximizing the triple-phase interface.[39]

To evaluate the mass-transport capability, the ORR and OER performances of the fabricated electrodes were further investigated using a triple-phase electrocatalytic system in 1 M KOH without O_2 pumping. One side of the electrode was immersed in the electrolyte, whereas the other side was connected to air through a superhydrophobic substrate (Figure S31, Supporting Information). In this case, O_2 diffused only from the ambient atmosphere. As shown in ORR LVS curves (Figure S32, Supporting Information), the Fe-N@CFs and Pt/C+Ir/C electrodes exhibited an apparent plateau, in which the current density was governed by the diffusion of O_2.[40] By contrast, the current density of Fe-N@Ni-HCFs continued to increase with a decrease in the applied potential. The superior ORR performance of the Fe-N@Ni-HCFs electrode in the triple-phase system can be attributed to its increased porosity and reasonable hydrophobicity. The partially wetted Fe-N@Ni-HCFs surface prevented the flooding of nanopores in the interior and enabled the trapping of O_2 and its rapid diffusion.[39a] Nonetheless, the Pt/C+Ir/C electrode fabricated by conventional drop-casting was surrounded by the electrolyte, and its performance mainly relied on the O_2 dissolved in the electrolyte. The Fe-N@CFs electrode has an insufficient reaction contact region and cannot ensure discontinuous O_2 delivery. Both cases result in inadequate triple-phase contact interfaces and, consequently, a lower current density. For the OER, the LSV curve of the Pt/C+Ir/C electrode showed a degraded growth rate of the current signal in the high-potential region (Figure S33, Supporting Information). The decreased reaction rate can probably be attributed to the sluggish escape of O_2, which hinders the electrolyte diffusion to the catalyst surface and even leads to the detachment of the catalyst.[41] In contrast, the Fe-N@Ni-HCFs electrode showed a relatively steady increase in the current, indicating the unimpeded reaction rate.[42] These results demonstrate the rapid mass transport in the Fe-N@Ni-HCFs electrode, which can be attributed to the wettability-balanced porous and hollow architecture that provides the desirable triple-phase contact

for electrocatalytic reactions and breathable tunnels for gas diffusion.

2.4. Zn–Air Battery Performances

Rechargeable ZABs were assembled using the Fe-N@Ni-HCFs electrode and Zn anode. ZABs with Fe-N@CFs and Pt/C+Ir/C electrodes were fabricated for comparison. The Fe-N@Ni-HCFs ZAB exhibited an open-circuit voltage (OCV) of 1.51 V (Figure 4d), which is higher than those of the Fe-N@CFs ZAB (1.42 V) and Pt/C+Ir/C ZAB (1.45 V). The electrocatalytic activity was further compared based on the discharge and charge polarization curves (Figure 4e). The narrower voltage gap of Fe-N@Ni-HCFs suggested better rechargeability, consistent with the excellent bifunctional ORR/OER activity observed in the three-electrode system. The corresponding power density of Fe-N@Ni-HCFs reached 172.2 mW cm^{-2} (Figure 4f), outperforming that of the commercial Pt/C+Ir/C couple (134.2 mW cm^{-2}). In contrast, the peak power density of Fe-N@CFs was limited to 128.2 mW cm^{-2} because of the insufficient active region. At the current density of 10 mA cm^{-2}, the Fe-N@Ni-HCFs ZAB delivered a specific capacity of 782.8 mAh g^{-1} (Figure S34, Supporting Information), which was higher than that of Pt/C+Ir/C (732.6 mAh g^{-1}).

To elaborate on the significant role of the hollow architecture, the hollow fiber structure of Fe-N@Ni-HCFs was mechanistically destroyed (Figure S35a, Supporting Information). A sluggish discharging behavior with reduced power density was observed in the discharge process of the ZAB with the cracked sample (Figure S35b, Supporting Information). Therefore, the rational structure design of Fe-N@Ni-HCFs to enlarge active regions and promote mass transfer are essential for improving the ZAB performance. The advantages of Fe-N@Ni-HCFs were more evident in the galvanostatic cycling test. As illustrated in Figure 4g, the ZAB with Fe-N@Ni-HCFs delivered initial discharge and charge voltages of 1.26 and 1.96 V at 10 mA cm^{-2}, respectively, corresponding to a round-trip efficiency of 64.3%. After continuous operation for 200 h, slight voltage fading was observed on Fe-N@Ni-HCFs, with discharge and charge voltages of 1.17 and 2.02 V, respectively. The round-trip efficiency was maintained at 57.9%. In contrast, the ZAB with Fe-N@CFs suffered from severe charge polarization during cycling because of its limited rechargeability. The Pt/C+Ir/C ZAB exhibited rapid performance fading, probably due to the exfoliation of noble metal nanoparticles and the collapse of the triple-phase interface.

As evident from the SEM image (Figure S36a, Supporting Information), the fibrous structure of Fe-N@Ni-HCFs with lotus root-like channels at the cross-section was well-preserved after cycling. Apart from metallic Ni and graphitic carbon peaks, no impurity peaks were observed in the XRD pattern of the cycled Fe-N@Ni-HCFs electrode (Figure S36b, Supporting Information). Thus, the post-operation characterizations demonstrated the excellent structural stability of Fe-N@Ni-HCFs, suggesting stable multiphase reactive regions and efficient active sites that could prolong the lifespan of ZABs.

Inspired by the flexible and robust features of Fe-N@Ni-HCFs, flexible quasi-solid-state (QSS) ZABs were assembled to explore their potential applications. **Figure 5**a illustrates the prototype of the flexible QSS ZABs, in which an alkaline polyvinyl alcohol (PVA) gel is used as the electrolyte. The assembled flexible QSS ZAB exhibited a stable OCV above 1.43 V in ambient air (Figure 5b). The power density of a single ZAB with the Fe-N@Ni-HCFs cathode reached 64.5 mW cm^{-2} (Figure 5c), which was higher than that of the Pt/C+Ir/C ZAB (53.1 mW cm^{-2}). Rate capability tests showed a narrower discharge-charge voltage gap for Fe-N@Ni-HCFs than for Pt/C+Ir/C at various current densities (Figure 5d), indicating its superior rate performance. Remarkably, the Fe-N@Ni-HCFs flexible battery could be operated in both flat and bent states (Figure 5e). The better cycling stability compared to that of the noble metal-based battery (Figure 5f) demonstrates the potential application of Fe-N@Ni-HCFs for wearable and portable devices.

The performances of the liquid and QSS ZABs with recently reported electrocatalysts were summarized in Tables S4 and S5 (Supporting Information), respectively. The developed Fe-N@Ni-HCFs electrode exhibited comparable or even better performances. The following factors can synergistically account for the outstanding performances of the Fe-N@Ni-HCFs electrode: 1) the quasi-core-shell structure of the Ni core and Fe–N_4–C shell prevents possible negative interference between the different active components. Alternatively, such an encapsulation structure increases the utilization efficiency of the reactive region and endows the catalyst with good durability. 2) The electronic coupling triggered by the encapsulated Ni nanoparticles alters the local charge distribution of the Fe–N_4 sites and boosts the intrinsic activity toward bifunctional ORR and OER. 3) The incorporation of Ni during the synthetic process results in the porous and hollow structure of Fe-N@Ni-HCFs, which enlarges the active area and provides more accessible active sites to participate in electrochemical reactions. 4) Mass transfer is significantly facilitated by the wettability-balanced porous structure, providing sufficient and stable triple-phase boundaries. 5) Blocking of the active sites can be avoided without adding a binder, and the interfacial contact resistance can also be reduced.

3. Conclusion

In summary, we have proposed the atomic modulation and structure design of atomic Fe–N_4 modified hollow carbon fibers with encapsulated Ni nanoparticles to promote ORR/OER bifunctional activity and mass transfer capability in rechargeable ZABs. DFT calculations revealed that the electronic coupling between the Fe–N_4–C shell and the underlying metallic Ni tuned the electronic configuration of the Fe–N_4 moieties and contributed to reduced energy barriers toward ORR and OER. Meanwhile, the porous hollow structure with lung bubble-like inner cavities enabled excellent mass transfer, establishing sufficient and stable triple-phase interfaces. The rational atomic modulation and structure design of Fe-N@Ni-HCFs resulted in small discharge–charge overpotentials, remarkable specific capacity, high power density, and satisfactory cycling stability of the rechargeable ZABs. The elaborated design concepts and strategies established in

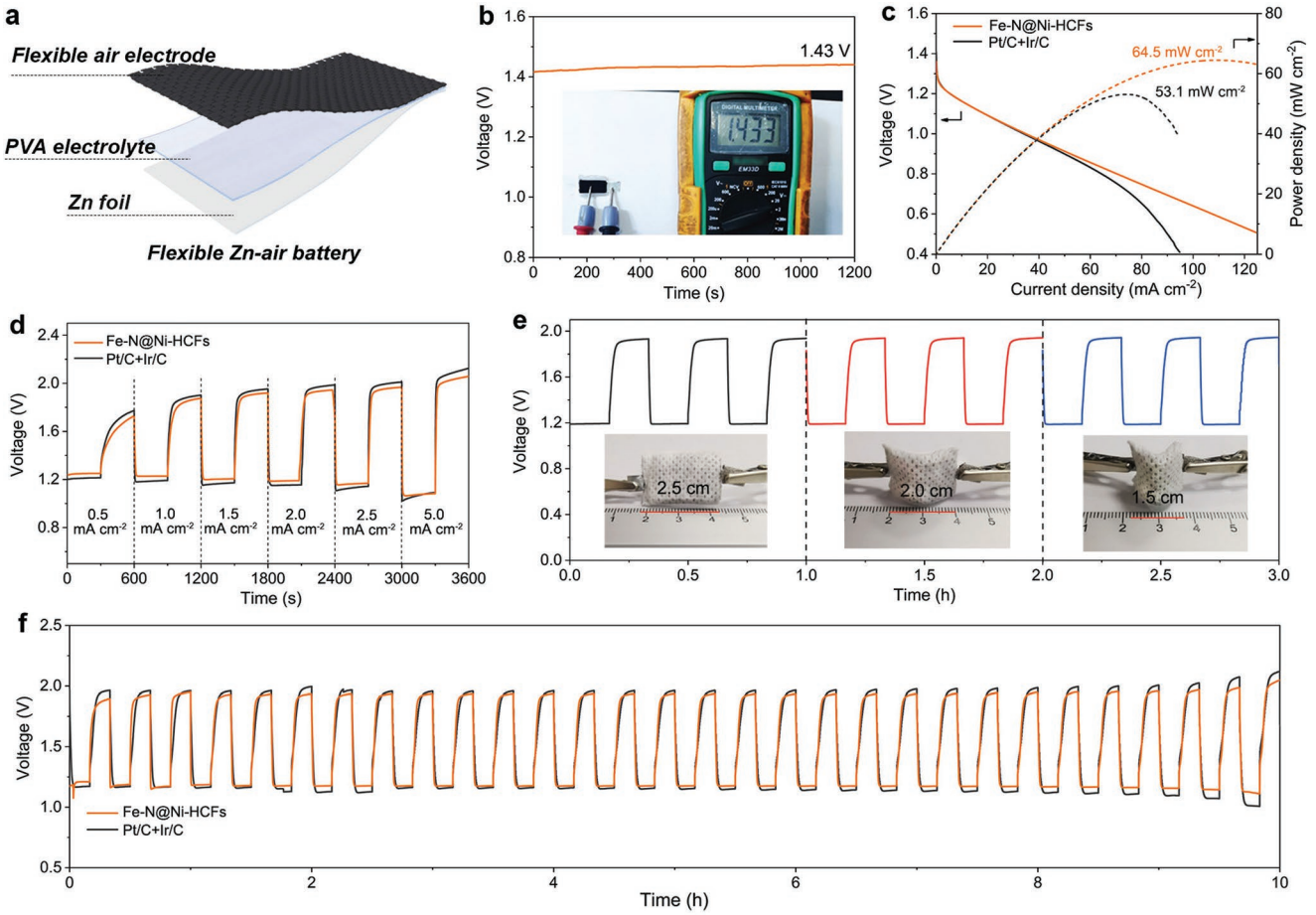

Figure 5. a) Schematic illustration for the configuration of the flexible QSS ZAB with PVA electrolyte. b) OCV plot of the as-assembled flexible ZAB with Fe-N@Ni-HCFs electrode (inset: photograph of the ZAB with the OCV of 1.433 V). c) Discharge polarization curves of flexible ZABs and corresponding power density plots. d) Comparison of galvanostatic discharge and charge curves for Pt/C+Ir/C and Fe-N@Ni-HCFs at different current densities. e) Discharge–charge cycling curve of the flexible ZAB with Fe-N@Ni-HCFs electrode at 2 mA cm^{-2} under different bending conditions. f) Galvanostatic discharge–charge cycling curves at 2 mA cm^{-2}.

this study are expected to advance the development of robust and high-performance catalyst materials for electrochemical energy conversion and storage devices.

Supporting Information

Supporting Information is available from the Wiley Online Library or from the author.

Acknowledgements

This work was financially supported by the Australian Research Council Discovery Project (grant No. DP210103266). The authors acknowledge the National Computational Infrastructure (NCI) National Facility systems at the Australian National University and the PAWSEY Supercomputing Centre located in Western Australia for providing computational resources. The authors are grateful to the Australian Synchrotron, part of Australia's Nuclear Science and Technology Organisation (ANSTO) in Melbourne, for providing XAS measurements. Y.T. would like to thank AINSE Ltd. for providing financial support (Postgraduate Research Award).

Open access publishing facilitated by Griffith University, as part of the Wiley - Griffith University agreement via the Council of Australian University Librarians.

Conflict of Interest

The authors declare no conflict of interest.

Data Availability Statement

The data that support the findings of this study are available from the corresponding author upon reasonable request.

Keywords

bifunctional oxygen electrocatalysts, binder-free electrodes, rechargeable Zn–air batteries, single-atom catalysts

Received: September 6, 2022
Published online: October 30, 2022

[1] a) Z. W. Seh, J. Kibsgaard, C. F. Dickens, I. Chorkendorff, J. K. Nørskov, T. F. Jaramillo, *Science* **2017**, *355*, 146; b) V. R. Stamenkovic, D. Strmcnik, P. P. Lopes, N. M. Markovic, *Nat. Mater.* **2016**, *16*, 57.
[2] J. Fu, Z. P. Cano, M. G. Park, A. Yu, M. Fowler, Z. Chen, *Adv. Mater.* **2017**, *29*, 1604685.
[3] M. Luo, W. Sun, B. B. Xu, H. Pan, Y. Jiang, *Adv. Energy. Mater.* **2021**, *11*, 2002762.
[4] M. Wu, G. Zhang, M. Wu, J. Prakash, S. Sun, *Energy Storage Mater.* **2019**, *21*, 253.
[5] M. Li, X. Bi, R. Wang, Y. Li, G. Jiang, L. Li, C. Zhong, Z. Chen, J. Lu, *Matter* **2020**, *2*, 32.
[6] Z. F. Huang, J. Wang, Y. Peng, C. Y. Jung, A. Fisher, X. Wang, *Adv. Energy Mater.* **2017**, *7*, 1700544.
[7] H. F. Wang, C. Tang, Q. Zhang, *Adv. Funct. Mater.* **2018**, *28*, 1803329.
[8] C. X. Zhao, J. N. Liu, B. Q. Li, D. Ren, X. Chen, J. Yu, Q. Zhang, *Adv. Funct. Mater.* **2020**, *30*, 2003619.
[9] Y. Tian, L. Xu, J. Qiu, X. Liu, S. Zhang, *Sustainable Mater. Technol.* **2020**, *25*, e00204.
[10] T. Zhou, N. Zhang, C. Wu, Y. Xie, *Energy Environ. Sci.* **2020**, *13*, 1132.
[11] M. Jiang, C. Fu, R. Cheng, W. Zhang, T. Liu, R. Wang, J. Zhang, B. Sun, *Adv. Sci.* **2020**, *7*, 2000747.
[12] V. Čolić, S. Yang, Z. Révay, I. E. L. Stephens, I. Chorkendorff, *Electrochim. Acta* **2018**, *272*, 192.
[13] T. Zhou, H. Shan, H. Yu, C. Zhong, J. Ge, N. Zhang, W. Chu, W. Yan, Q. Xu, H. Wu, C. Wu, Y. Xie, *Adv. Mater.* **2020**, *32*, 2003251.
[14] a) S. Kattel, P. Atanassov, B. Kiefer, *J. Phys. Chem. C* **2012**, *116*, 8161; b) X. Yang, D. Xia, Y. Kang, H. Du, F. Kang, L. Gan, J. Li, *Adv. Sci.* **2020**, *7*, 2000176; c) L. Zhao, Y. Zhang, L. B. Huang, X. Z. Liu, Q. H. Zhang, C. He, Z. Y. Wu, L. J. Zhang, J. Wu, W. Yang, L. Gu, J. S. Hu, L. J. Wan, *Nat. Commun.* **2019**, *10*, 1278; d) L. Jiao, J. Li, L. L. Richard, Q. Sun, T. Stracensky, E. Liu, M. T. Sougrati, Z. Zhao, F. Yang, S. Zhong, H. Xu, S. Mukerjee, Y. Huang, D. A. Cullen, J. H. Park, M. Ferrandon, D. J. Myers, F. Jaouen, Q. Jia, *Nat. Mater.* **2021**, *20*, 1385.
[15] C. X. Zhao, B. Q. Li, J. N. Liu, Q. Zhang, *Angew. Chem., Int. Ed.* **2021**, *60*, 4448.
[16] a) Q. Zhang, P. Kumar, X. Zhu, R. Daiyan, N. M. Bedford, K. H. Wu, Z. Han, T. Zhang, R. Amal, X. Lu, *Adv. Energy Mater.* **2021**, *11*, 2100303; b) Z. Wang, C. Zhu, H. Tan, J. Liu, L. Xu, Y. Zhang, Y. Liu, X. Zou, Z. Liu, X. Lu, *Adv. Funct. Mater.* **2021**, *31*, 2104735.
[17] G. K. Mao, C. Yan, Z. Zhu, A. Du, *J. Phys. Chem. C* **2019**, *123*, 3703.
[18] I. S. Amiinu, X. Liu, Z. Pu, W. Li, Q. Li, J. Zhang, H. Tang, H. Zhang, S. Mu, *Adv. Funct. Mater.* **2018**, *28*, 1704638.
[19] M. Xiao, Z. Xing, Z. Jin, C. Liu, J. Ge, J. Zhu, Y. Wang, X. Zhao, Z. Chen, *Adv. Mater.* **2020**, *32*, 2004900.
[20] a) S. Liu, Z. Wang, S. Zhou, F. Yu, M. Yu, C. Y. Chiang, W. Zhou, J. Zhao, J. Qiu, *Adv. Mater.* **2017**, *29*, 1700874; b) T. Duguet, E. Gaudry, T. Deniozou, J. Ledieu, M. C. de Weerd, T. Belmonte, J. M. Dubois, V. Fournée, *Phy. Rev. B* **2009**, *80*, 205412.
[21] Y. Wang, Y. J. Tang, K. Zhou, *J. Am. Chem. Soc.* **2019**, *141*, 14115.
[22] Y. Zhou, X. Tao, G. Chen, R. Lu, D. Wang, M. X. Chen, E. Jin, J. Yang, H. W. Liang, Y. Zhao, X. Feng, A. Narita, K. Müllen, *Nat. Commun.* **2020**, *11*, 5892.
[23] M. Jia, C. Choi, T. S. Wu, C. Ma, P. Kang, H. Tao, Q. Fan, S. Hong, S. Liu, Y. L. Soo, Y. Jung, J. Qiu, Z. Sun, *Chem. Sci.* **2018**, *9*, 8775.
[24] G. Prieto, H. Tuysuz, N. Duyckaerts, J. Knossalla, G. H. Wang, F. Schuth, *Chem. Rev.* **2016**, *116*, 14056.
[25] Z. Qiao, C. Wang, C. Li, Y. Zeng, S. Hwang, B. Li, S. Karakalos, J. Park, A. J. Kropf, E. C. Wegener, Q. Gong, H. Xu, G. Wang, D. J. Myers, J. Xie, J. S. Spendelow, G. Wu, *Energy Environ. Sci.* **2021**, *14*, 4948.
[26] a) R. Liu, Z. Gong, J. Liu, J. Dong, J. Liao, H. Liu, H. Huang, J. Liu, M. Yan, K. Huang, H. Gong, J. Zhu, C. Cui, G. Ye, H. Fei, *Adv. Mater.* **2021**, *33*, 2103533; b) C. Hu, C. Yu, M. Li, X. Wang, Q. Dong, G. Wang, J. Qiu, *Chem. Commun.* **2015**, *51*, 3419.
[27] L. Xu, Y. Tian, D. Deng, H. Li, D. Zhang, J. Qian, S. Wang, J. Zhang, H. Li, S. Sun, *ACS Appl. Mater. Interfaces* **2020**, *12*, 31340.
[28] Y. Yan, S. Liang, X. Wang, M. Zhang, S. M. Hao, X. Cui, Z. Li, Z. Lin, *Proc. Natl. Acad. Sci. USA* **2021**, *118*, e2110036118.
[29] H. Yin, P. Yuan, B. A. Lu, H. Xia, K. Guo, G. Yang, G. Qu, D. Xue, Y. Hu, J. Cheng, S. Mu, J. N. Zhang, *ACS Catal.* **2021**, *11*, 12754.
[30] Y. Pan, Y. Chen, K. Wu, Z. Chen, S. Liu, X. Cao, W. C. Cheong, T. Meng, J. Luo, L. Zheng, C. Liu, D. Wang, Q. Peng, J. Li, C. Chen, *Nat. Commun.* **2019**, *10*, 4290.
[31] Y. Tsao, H. Gong, S. Chen, G. Chen, Y. Liu, T. Z. Gao, Y. Cui, Z. Bao, *Adv. Energy Mater.* **2021**, *11*, 2101449.
[32] X. Xie, L. Peng, H. Yang, G. I. N. Waterhouse, L. Shang, T. Zhang, *Adv. Mater.* **2021**, *33*, 2101038.
[33] a) X. Ge, G. Su, W. Che, J. Yang, X. Zhou, Z. Wang, Y. Qu, T. Yao, W. Liu, Y. Wu, *ACS Catal.* **2020**, *10*, 10468; b) H. L. Fei, J. C. Dong, Y. X. Feng, C. S. Allen, C. Z. Wan, B. Volosskiy, M. F. Li, Z. P. Zhao, Y. L. Wang, H. T. Sun, P. F. An, W. X. Chen, Z. Y. Guo, C. Lee, D. L. Chen, I. Shakir, M. J. Liu, T. D. Hu, Y. D. Li, A. I. Kirkland, X. F. Duan, Y. Huang, *Nat. Catal.* **2018**, *1*, 63.
[34] Y. Fan, C. Zhuang, S. Li, Y. Wang, X. Zou, X. Liu, W. Huang, G. Zhu, *J. Mater. Chem. A* **2021**, *9*, 1110.
[35] Y. Tian, X. Liu, L. Xu, D. Yuan, Y. Dou, J. Qiu, H. Li, J. Ma, Y. Wang, D. Su, S. Zhang, *Adv. Funct. Mater.* **2021**, *31*, 2101239.
[36] Y. Chen, S. Ji, S. Zhao, W. Chen, J. Dong, W. C. Cheong, R. Shen, X. Wen, L. Zheng, A. I. Rykov, S. Cai, H. Tang, Z. Zhuang, C. Chen, Q. Peng, D. Wang, Y. Li, *Nat. Commun.* **2018**, *9*, 5422.
[37] J. Yu, B. Q. Li, C. X. Zhao, J. N. Liu, Q. Zhang, *Adv. Mater.* **2020**, *32*, 1908488.
[38] P. Wang, T. Hayashi, Q. Meng, Q. Wang, H. Liu, K. Hashimoto, L. Jiang, *Small* **2017**, *13*, 1601250.
[39] a) M. Qiao, C. Tang, L. C. Tanase, C. M. Teodorescu, C. Chen, Q. Zhang, M. M. Titirici, *Mater. Horiz.* **2017**, *4*, 895. b) H. Jiang, R. Luo, Y. Li, W. Chen, *EcoMat* **2022**, *4*, e12199.
[40] W. Xia, A. Mahmood, Z. Liang, R. Zou, S. Guo, *Angew. Chem., Int. Ed.* **2016**, *55*, 2650.
[41] a) R. A. Rincon, E. Ventosa, F. Tietz, J. Masa, S. Seisel, V. Kuznetsov, W. Schuhmann, *ChemPhysChem* **2014**, *15*, 2810. b) X. Lu, C. Zhao, *Nat. Commun.* **2015**, *6*, 6616.
[42] J. Li, Y. Zhu, W. Chen, Z. Lu, J. Xu, A. Pei, Y. Peng, X. Zheng, Z. Zhang, S. Chu, Y. Cui, *Joule* **2018**, *3*, 557.